Fusion and elastic scattering of $^{20}Ne + ^{40}Ca$

Nguyen Van Sen, R. Darves-Blanc, J. C. Gondrand, and F. Merchez
Institut des Sciences Nucléaires, IN2P3 and U.S.M.G., B.P. 257, 38026 Grenoble, France
(Received 5 March 1979)

Fusion and elastic scattering cross sections were measured for ^{20}Ne bombardments of ^{40}Ca from 44 to 70 MeV. The evaporation residues from the compound nucleus decay were detected by a gas counter telescope. The fusion data were compared to results for $^{16}O + ^{40}Ca$ within the framework of the proximity, the Siwek-Wilczynska and Wilczynski, and the folding model potentials. Although the ratio σ_{fus}/σ_R is appreciably lower for ^{20}Ne than for ^{16}O, consistent results were obtained for σ_{fus} within the experimental uncertainties.

[NUCLEAR REACTIONS $^{20}Ne + ^{40}Ca$, $E = 44.1$ to 70.4 MeV; Measured evaporation residue $\sigma(E, \theta)$. Deduced $\sigma(E)$ total fusion excitation functions. Measured elastic scattering $\sigma(\theta)$. Natural target. Deduced ion-ion potentials.]

I. INTRODUCTION

The relationship between the elastic scattering and the total reaction cross sections for heavy ions has been widely investigated.[1,2] Optical model fits of the elastic scattering or even the classical Blair quarter-point recipe[3] can furnish a reasonable estimate of the reaction cross section σ_R. However, direct accurate measurements of σ_R are rather difficult in contrast to the fusion cross section σ_{fus}. Mostly with gas counter telescopes, a large body of fusion data[2] has been obtained with good accuracy in the last few years. For small Z_1Z_2 systems at low energies, it has been often assumed that $\sigma_{fus} \approx \sigma_R$; thus the fusion barrier deduced from theoretical analyses[1,4] is nearly indistinguishable from the reaction barrier. In fact, the ratio of σ_{fus} to σ_R might depend on the nuclear structure effects which give rise in some cases to a noticeable contribution from processes occurring at the nuclear surface, such as inelastic scattering or transfer reactions.

In a recent study of the system $^{16}O + ^{40}Ca$, Geesaman *et al.*[5] have shown that the fusion cross section in the energy range 45 to 63 MeV accounted for about 90% of the σ_R calculated from the optical model fit of the elastic scattering. It has been observed in a previous work[6] on the ^{20}Ne scattering from ^{40}Ca in a similar energy range that the inelastic scattering cross sections for excitation of the lower collective states of the projectile and the target exhausted about 20% of the σ_R deduced from the elastic scattering. If the contributions from other peripherial processes are also included, the ratio σ_{fus}/σ_R is expected to be appreciably lower for ^{20}Ne than for ^{16}O. Within the framework of recent theoretical models based on universal ion-ion potentials[7,8] there should, nevertheless, be some consistency between the fusion data for the two systems. The purpose of the present work was to look into this consistency by measuring the fusion cross section for $^{20}Ne + ^{40}Ca$ from 44 to 70 MeV. The comparison with the ^{16}O data was performed through calculations using the proximity[7] and the Siwek-Wilczynska and Wilczynski[8] potentials together with the Hill and Wheeler parabolic approximation.[9] Calculations were also done with the folding model by the Brink and Rowley method.[10]

Elastic scattering angular distributions for $^{20}Ne + ^{40}Ca$ were also measured simultaneously with the fusion. The data were analyzed in terms of the optical model. The interaction barrier deduced from the real part of the optical potential was compared to the results obtained from the preceding models.

II. EXPERIMENTAL PROCEDURE

The measurements were performed inside a 1 m diam scattering chamber, for both the elastic scattering and the evaporation residues following complete fusion. Self-supporting natural Ca targets 100 $\mu g/cm^2$ thick were bombarded with ^{20}Ne beams provided by the Grenoble isochronous cyclotron. A collimator composed of three successive tantalum slits limited the focused beam spot at the target position to about 3 mm in diameter. Beam intensities from a few nA to 200 nA were collected during the experiments by a Faraday cup placed downstream of the scattering chamber.

The elastic spectra were obtained by means of five Si surface-barrier detectors mounted at 8° lab intervals on an arm movable around the target. Each detector has in the lab frame an angular acceptance of about 0.5° and a solid angle of about 0.15 msr. The angular uncertainty on the detection angle was about ±0.05°. Two solid-state monitor detectors were placed at fixed angles in the forward hemisphere of the chamber in order to

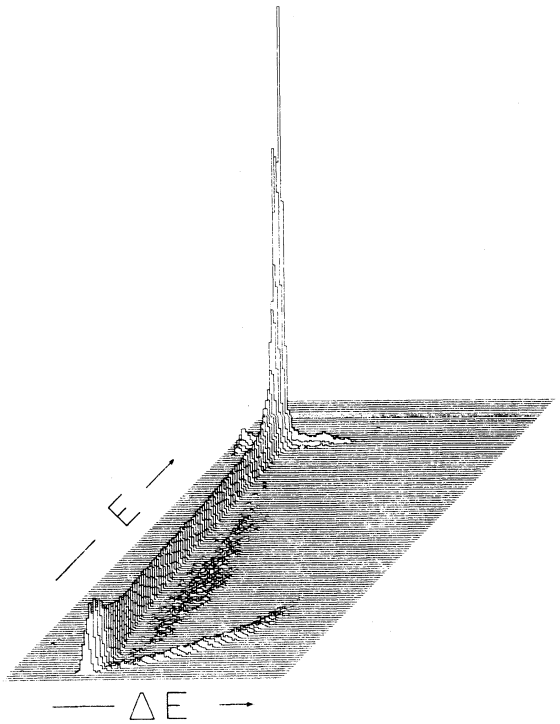

FIG. 1. E-ΔE spectrum at 63 MeV and 8° lab. The square root of the yield is presented in the vertical scale for events having more than one count. The mountain of events with large ΔE and low E belongs to the evaporation residues from the $^{20}Ne+^{40}Ca$ fusion.

obtain the relative normalization for the measured angular distributions, and to control the stability of the beam energy and the position of the beam spot on the target. The absolute values of the cross section were obtained by normalizing the elastic scattering data at forward angles to the calculated Rutherford cross section.

The evaporation residues were detected on the opposite side of the beam direction by a gas-flow proportional counter having a low resistivity Si detector on its internal rear side. The proportional counter consisted of a single tungsten wire centered along the axis of a 5.5 cm long, 2 cm diam cylinder. The counter was run with a mixture of 90% Ar +10% CH_4 gas at constant pressures giving thicknesses of about 200 $\mu g/cm^2$ and with a Parylen-C (Ref. 11) entrance window, 0.3 μm thick. The solid angle of the ΔE counter was limited to about 0.1 msr in order to permit accurate measurements at small forward angles and to account for the multiple scattering of the heavy products in the gas of the counter. The ΔE-E spectra were analyzed in 128×128 channel arrays by a conventional multichannel analyzer and recorded on magnetic tapes by means of a PDP-9 computer. A typical spectrum is shown in Fig. 1 where the evaporation residues from complete fusion of $^{20}Ne+^{40}Ca$ are clearly identified at the bottom right part and well separated from the lighter products. The spectra were, however, worsened at very small forward angles because of the huge yield of ^{20}Ne and some contribution from the fusion of ^{20}Ne with carbon and oxygen contaminants on the target. The measurements were discarded whenever the yield of the evaporation products could not be obtained with an accuracy better than 10%. The relative angular distributions were obtained by using the monitor detector counting, whereas the absolute values were deduced from the ratio of the fusion to the elastic yields.

III. EXPERIMENTAL RESULTS

From the E-ΔE spectrum of the gas counter telescope, the fusion mountain could be converted into an energy distribution. Pulse-height defects for heavy ions in the Si surface-barrier detector were corrected using the methods in Refs. 12 and 13. Energy losses in the target, the Parylen entrance window, and the dead layers of the Si detector were also taken into account by means of the Northcliffe and Schilling stopping powers.[14] Some typical energy spectra are shown in Fig. 2; the accuracy of the energy scale is about ±1 MeV. The residues are peaked at roughly the same velocity as the original compound nucleus.

Fusion angular distributions obtained from 4° to 24° lab are shown in Fig. 3. In order to get the angle-integrated cross section $\sigma_{fus}(E)$, the angular distribution was extrapolated into the forward region not measured by fitting the data in the range 0°–8° with the equation

$$d\sigma_{fus}/d\Omega = a\sin^2\theta + b\,.$$

This form is roughly consistent with the statistical model calculations.[15] The $\sigma_{fus}(E)$ is actually obtained by finding the area under the curve $d\sigma/d\theta$ vs θ, so that the uncertainty due to the extrapolation procedure is less than a few percent. An example of $d\sigma/d\theta$ is shown in the inset on Fig. 3. The integrated $\sigma_{fus}(E)$ plotted in Fig. 5 have an accuracy of about 5–8%, taking into account the statistical uncertainty, the absolute normalization, and the extrapolation procedure errors.

The elastic scattering angular distributions obtained from 44.1 to 70.4 MeV are plotted in Fig. 7. The relative errors are about ±5% including statistical and background subtraction uncertainties (±4%), and absolute normalization errors (±3%). The numerical data can be obtained from Ref. 22 for the fusion and elastic scattering cross sections illustrated in Figs. 5 and 7.

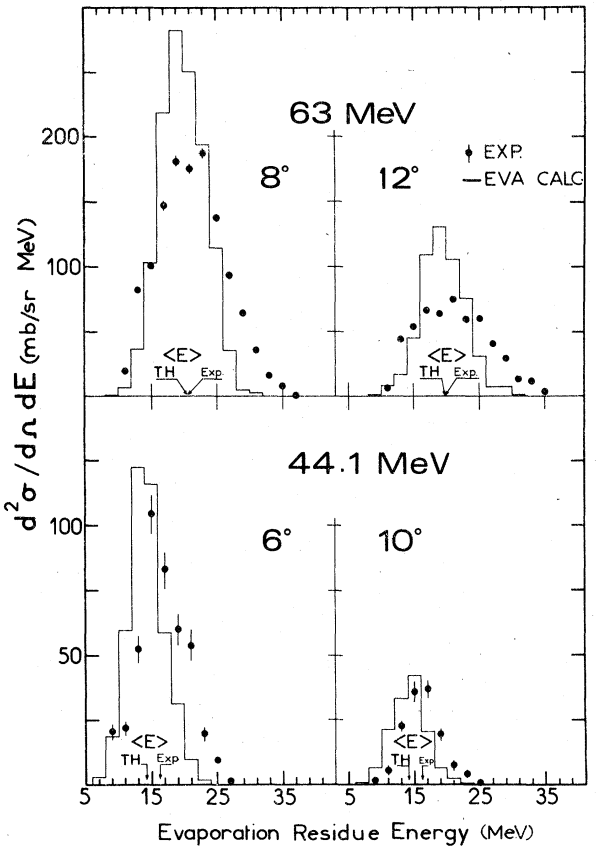

FIG. 2. Typical energy spectra of the evaporation residues compared to the statistical model calculations using the EVA code (Ref. 15). The arrows indicate the theoretical (TH) and experimental (Exp) centroid energies.

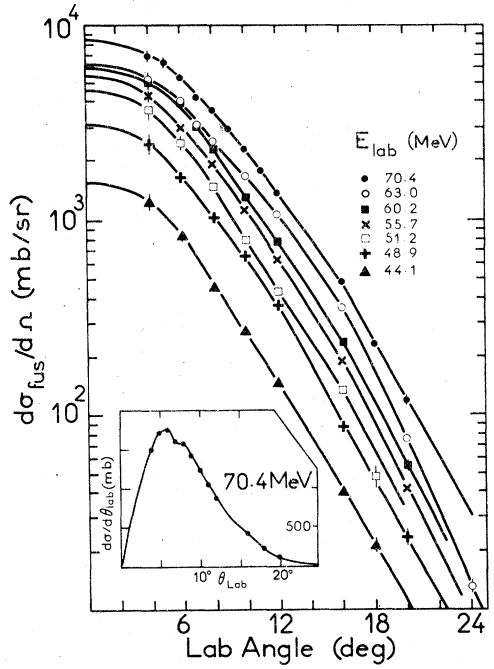

FIG. 3. Fusion angular distributions for $^{20}Ne + ^{40}Ca$. The solid curves guide the eye through the experimental points. Extrapolation at forward angles is performed with $d\sigma/d\Omega = a\sin^2\theta + b$ (see text). An example of $d\sigma/d\theta$ distribution used to obtain the angle-integrated $\sigma_{fus}(E)$ is shown in the inset.

IV. THEORETICAL ANALYSIS

A. Fusion

Theoretical calculations of the fusion energy spectra were carried out using the statistical model by means of the EVA code[15] which is an improved version of the DFF evaporation code.[16] It was assumed that a complete equilibration of the excitation energy is reached among the constituents of the Zn compound nucleus. Emissions of n, p, d, t, ^{3}He, and α were considered in the cascade calculations. The evaporation particles were assumed to be emitted isotropically in the center-of-mass frame. The simple Fermi-gas formula was used for the level density with a level-density parameter $a = A/8$, where A is the mass of the decaying nucleus.

Four typical calculated spectra are compared with the experimental data in Fig. 2. The theoretical results are normalized so as to have the area under the curve equal to the fusion cross section. The arrows on the energy axis mark the centroid energies $\langle E\rangle = \Sigma n_i E_i / \Sigma n_i$ of the distributions. At 63 MeV a good agreement was obtained for the $\langle E\rangle$ whereas the width of the calculated distribution is slightly narrower than the experimental data. At 44.1 MeV a better agreement was obtained for the distribution width, while the theoretical $\langle E\rangle$ was shifted to lower energy by about 2 MeV; this shift is not really conclusive in light of the experimental scale uncertainty.

The statistical model calculations for the angular distributions are compared with the data in Fig. 4. Because the EVA code did not provide the absolute cross section, the calculations are normalized to the experiment at the forward angles. At angles larger than 10° the theoretical angular distribution has a slope steeper than the experiment. Attempts made to improve the fits by variations of the level density parameter did not give conclusive differences. These discrepancies are probably due to the large angular momentum of the compound nucleus, which favors the emission of composite particles. The yield of those particles is underestimated in the present evaporation calculations which do not take into account the angular momentum effects. Because the yield at large angle is determined kinematically by the contribution from

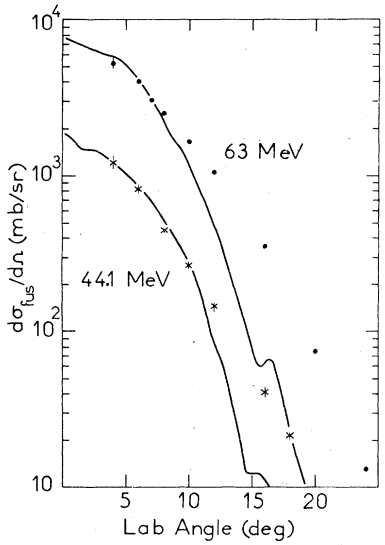

FIG. 4. Comparison of the fusion angular distributions for ^{20}Ne+^{40}Ca at 44.1 and 63 MeV with the statistical model calculations (Ref. 15).

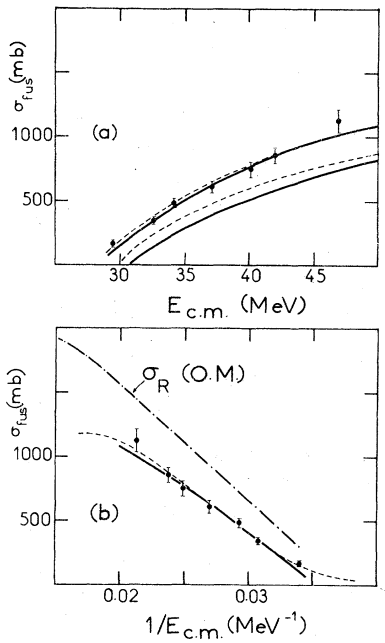

FIG. 5. Fusion energy excitation function for ^{20}Ne +^{40}Ca compared to theoretical calculations. (a) solid line: proximity potential calculations with $r_0 = 1.28$ fm in Eq. (4) (lower curve) and $r_0 = 1.37$ fm (upper); dashed line: SWW potential with $r_0 = 1.128$ fm in Eq. (8) (lower) and $r_0 = 1.241$ fm (upper). (b) solid line: folding model calculations; dashed line: Glas-Mosel calculations; dash-and-dotted line: average trend of the total reaction cross section.

the light evaporation residues, the theoretical angular distribution decreases more quickly than the experiment.

The fusion energy excitation functions were compared to calculations[8] assuming that fusion occurs when the ion-ion potential barrier B_l has been passed. Thus the fusion cross section is

$$\sigma_{fus} = \pi\lambda^2 \sum_l (2l+1) T_l , \tag{1}$$

where λ is the reduced wavelength, and T_l is the transmission coefficient which is calculated via the Hill-Wheeler parabolic approximation.[9]

For each orbital angular momentum l it was assumed that the ion-ion potential consists of the sum of the point charge Coulomb potential, the centrifugal component, and the nuclear potential.

The nuclear potential cannot be determined without ambiguity from the elastic scattering data which are sensitive only to a narrow part of the potential tail around the strong absorption radius. The fusion process, even at low energies, is sensitive to closer distances, particularly to the height and shape of the interaction barrier. Several universal ion-ion potentials have been derived in the last few years.[7,8,17]

By assuming that the range of the nuclear force is short in comparison with nuclear dimensions, Blocki *et al.*[7] have shown that the ion-ion potential is given by

$$V_N(\zeta) = 4\pi\gamma \frac{C_p C_T}{C_p + C_T} b \Phi(\zeta) , \tag{2}$$

where

$$\gamma = 0.9517(1 - 1.7826 I^2)\ \text{MeV/fm}^2 ,$$

$$I = (N_p + N_T - Z_p - Z_T)/(A_p + A_T) .$$

C_p and C_T are the half-density nuclear radii for the projectile and the target, respectively. C is related to the equivalent sharp radius by

$$C_i = R_i[1 - (b/R_i)^2 + \ldots] , \tag{3}$$

where $b \approx 1$ fm is the surface width, and

$$R_i = r_0 A_i^{1/3} - 0.76 + 0.8 A_i^{-1/3} . \tag{4}$$

The function $\Phi(\zeta)$ is expressed in terms of the separation distance ζ between the half-density surfaces

$$\zeta = (r - C_p - C_T)/b$$

by means of a universal cubic-exponential formula.[7]

Calculations performed with the proximity potential in Eq. (2) for ^{20}Ne +^{40}Ca are compared to the experimental data in Fig. 5(a). The theoretical results are about 35% lower than the measured data if $r_0 = 1.28$ fm as recommended by Blocki *et al.*[7] In order to fit the data, r_0 had to be $r_0 = 1.37$ fm, as shown by the upper solid line in Fig. 5(a). Similar results were obtained for the ^{16}O +^{40}Ca

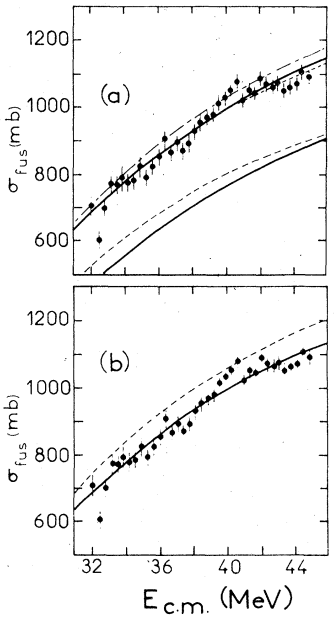

FIG. 6. Fusion energy excitation function (Ref. 5) for $^{16}O+^{40}Ca$ compared to theoretical calculations. (a) proximity potential calculations with $r_0=1.28$ fm in Eq. (4) (lower solid curve), $r_0=1.36$ fm (upper solid curve), and $r_0=1.37$ fm (dash-and-dotted curve); SWW calculations with $r_0=1.128$ fm in Eq. (8) (lower dashed curve) and $r_0=1.241$ fm (upper). (b) folding model calculations with $r_T=1.06$ fm (solid curve) and $r_T=1.10$ fm (dashed curve).

fusion data taken from Geesaman *et al.*[5] The best fit was obtained in Fig. 6(a) with nearly the same r_0 as for the ^{20}Ne data, that is, $r_0=1.36$ fm.

Theoretical calculations were also carried out with another potential derived by Siwek-Wilczynska and Wilczynski (SWW)[8] from the liquid drop model. The potential is postulated to have a Woods-Saxon form

$$V(r)=-V_0\{1+\exp[(r-C_p-C_T)/a]\}^{-1}, \tag{5}$$

with

$$V_0=b_{surf}[A_p^{2/3}+A_T^{2/3}-(A_p+A_T)^{2/3}], \tag{6}$$

where $b_{surf}\approx 17$ MeV is the surface energy parameter. Moreover, the maximum force acting between the two nuclei is supposed to be

$$\left(\frac{dV}{dr}\right)_{r=C_p+C_T}=\frac{V_0}{4a}=4\pi\gamma\frac{C_pC_T}{C_p+C_T}. \tag{7}$$

The half-density radii C_p and C_T are given by

$$C_i=r_0A_i^{1/3}(1-0.786A_i^{-2/3}),\quad r_0=1.128\text{ fm}. \tag{8}$$

The diffuseness is obtained from Eq. (7).

Calculations were performed for both the $^{20}Ne+^{40}Ca$ and $^{16}O+^{40}Ca$ fusions using the SWW potential in Eq. (5). Comparisons with the experimental data are shown in Figs. 5 and 6. The calculated values are clearly lower than the experimental data, unless a larger r_0 is used in Eq. (8). Good agreement was obtained with $r_0=1.241$ fm in both Figs. 5(a) and 6(a). These results are consistent with the proximity potential calculations. For both the models, radii of $C_P+C_T\approx 1.13\ (A_p^{1/3}+A_T^{1/3})$ fm had to be used instead of the original values.

Another potential which was studied in the present analysis is the folding model potential. The interaction potential between two nuclei whose densities do not overlap too much can be calculated by folding the nuclear density distribution of one nucleus with the real part of the single-nucleon optical potential of the other. If the nucleon density distribution and the single-nucleon optical potential are assumed to have Woods-Saxon form factors, analytic approximations[10] can be derived for the folded potential and its derivative for large separations of the interacting nuclei. These approximations should be valid in the region of the interaction barrier so that a simple iteration procedure allows one to deduce the height, the position, and the shape of the barrier B_l from $l=0$ to $l=l_c$, l_c being the critical angular momentum defined as the angular momentum l_c for which the projectile just surmounts the barrier provided by the sum of the Coulomb and centrifugal potentials and the real part of the nuclear potential.

The critical angular momentum l_c has been originally[10] derived from the elastic scattering experimental cross sections by using the classical relationship[2]

$$l_c\approx l_{1/4}=\eta\cot(\theta_{1/4}/2), \tag{9}$$

where η is the Sommerfeld parameter and $\theta_{1/4}$ is the angle at which the observed cross section has fallen to $\frac{1}{4}$ of the Rutherford result. In fact, the angular momentum deduced from Eq. (9) is related to the total reaction cross section which, in addition to the fusion process, takes into account the peripheral reactions occurring on the tail of the ion-ion potential.

It might be more suitable to use the fusion cross section in order to obtain the critical angular momentum used in the folding model.[10] Equation (1) could be reduced to

$$\sigma_{fus}=\pi\lambda^2(l_c+1)^2 \tag{10}$$

by using the sharp cutoff approximation, i.e., $T_l=1$ for $l\leq l_c$ and $T_l=0$ for $l\geq l_c$. Calculations following such a procedure were performed for the $^{20}Ne+^{40}Ca$ and the $^{16}O+^{40}Ca$ data. The same parametrization as in Ref. 10 was adopted. The Woods-Saxon shape of the projectile has a radius $R_p=1.04A_p^{1/3}$ fm, a diffuseness $a_p=0.54$ fm, and a central density

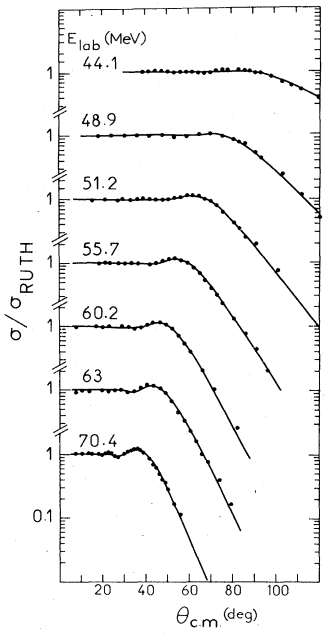

FIG. 7. Elastic scattering angular distributions for ^{20}Ne+^{40}Ca compared to the optical model calculations with parameters in Table I.

$$\rho_0 = 0.212(1+2.66A_p^{-2/3})^{-1}\text{fm}^{-3}.$$

The single-nucleon potential for the target nucleus has a Woods-Saxon form factor with depth $V_T = 50$ MeV, diffuseness $a_T = 0.65$ fm, and radius $R_T = r_T A_T^{1/3}$, where r_T is taken to be a free parameter. The radius r_T is searched in order to get for the folded potential a critical angular momentum l_c equal to the value deduced from the fusion data through Eq. (10). The best fits were obtained with $r_T = 1.10 \pm 0.03$ fm. Calculations performed with the average r_T are shown by the solid line in Fig. 5(b). With the same radius, the theoretical results for the system ^{16}O+^{40}Ca are about 5% higher than the experimental data. Very good agreement with the data can be obtained with a slightly lower value, $r_T = 1.06$ fm.

If Eq. (9) had been used to deduce the critical angular momentum from the quarter-points of the elastic scattering shown in Fig. 7, radii of $r_T = 1.25$–1.30 fm would be obtained for the ^{20}Ne+^{40}Ca folded potential, similar to previous results for Ge targets.[19]

The Glas-Mosel model[4] was also used to fit the ^{20}Ne+^{40}Ca experimental data. The dashed curve shown in Fig. 5(b) was obtained with $V_B = 28.60$ MeV, $R_B = 9.34$ fm, $\hbar\omega = 10$ MeV, the high-energy parameters being arbitrarily fixed to $V_{cr} = 0$ MeV, $R_{cr}/(A_p^{1/3}+A_T^{1/3}) = 1$ fm. The large $\hbar\omega$ might reflect effects[20] due to the large deformation of ^{20}Ne; more measurements near the Coulomb barrier will be needed in order to clarify this point.

B. Elastic scattering

The elastic scattering angular distributions were analyzed in terms of the optical model. Calculations were performed with the SPI code[18] using a four-parameter potential

$$U(r) = V_{\text{Coul}} - \frac{(V+iW)}{1+\exp\{[r-r_0(A_p^{1/3}+A_T^{1/3})]/a\}},$$

where V_{Coul} is the Coulomb potential for a uniformly charged sphere of the same radius as the complex nuclear part.

The determination of the nuclear potential strength is actually subject to ambiguities, so that V could be fixed arbitrarily. In order to compare the ion-ion potential obtained from the elastic scattering with the SWW potential, Eq. (6) was used to calculate the strength V which is $V = 65.54$ MeV for ^{20}Ne+^{40}Ca.

For each angular distribution a gridding search was made for the imaginary depth. For a chosen value of W in the range 0–65 MeV the χ^2 minimization was performed by adjusting r_0 and a. The

TABLE I. Optical model parameters [a] for ^{20}Ne+^{40}Ca. The total reaction cross sections σ_R deduced from the elastic scattering fits and the fusion cross section $\sigma_{\text{fus}}^{\text{OM}}$ calculated from the real part of the optical potential are compared to the experimental fusion data.

E_{lab} (MeV)	r (fm)	a (fm)	σ_R (mb)	$\sigma_{\text{fus}}^{\text{OM}}$ (mb)	$\sigma_{\text{fus}}^{\text{exp}}$ (mb)
44.1	1.176	0.69	338	132	160 ± 20
48.9	1.137	0.716	577	325	340 ± 25
51.2	1.207	0.666	769	531	477 ± 30
55.7	1.180	0.68	931	656	605 ± 45
60.2	1.199	0.679	1145	844	743 ± 60
63	1.203	0.669	1227	921	852 ± 60
70.4	1.195	0.681	1436	1078	1121 ± 90

[a] With $V = 63.54$ MeV (see text) and $W = 40$ MeV. The energy-averaged radius and diffuseness are $\langle r\rangle = 1.18 \pm 0.02$ fm and $\langle a\rangle = 0.68 \pm 0.02$ fm.

TABLE II. Height and position of the interaction barrier for $^{20}Ne + ^{40}Ca$.

Model	V_B (MeV)	r_B (fm)	$V_N(R_B)$ (MeV) [a]
Proximity	28.3	1.53	−2.46
SWW	28.0	1.53	−2.64
Folding	28.7	1.52	−2.52
Glas-Mosel	28.6	1.52	−2.24
OM[b]	28.0	1.55	−2.25

[a] Nuclear potential at the barrier maximum, $R_B = r_B (A_p^{1/3} + A_T^{1/3})$.

[b] Energy-averaged values $V_B = 28.0 \pm 0.3$ MeV, $r_B = 1.55 \pm 0.03$ fm, and $V_N = -2.25 \pm 0.10$ MeV.

best fits could be obtained with W around 40 MeV, so that W was also fixed to this value and only r_0 and a were adjusted in order to get the fits shown in Fig. 7. The parameters r_0 and a so obtained are reported in Table I. Their average values $\langle r \rangle = 1.18 \pm 0.02$ fm and $\langle a \rangle = 0.68 \pm 0.02$ fm differ by about 10% from the SWW potential parameters deduced from the best fit of the $^{20}Ne + ^{40}Ca$ fusion excitation function, namely, $r_0 = (C_p + C_T)/(A_p^{1/3} + A_T^{1/3}) = 1.136$ fm and $a = 0.777$ fm.

Also reported in Table I are the total reaction cross sections σ_R, together with the fusion cross sections σ_{fus}^{OM} calculated from the real part of the optical potential by using Eq. (1). The σ_{fus}^{OM} are in fair agreement with the measured data σ_{fus}^{exp}. The average trend of σ_R is plotted in Fig. 5(b). The σ_{fus}^{exp} account for about 65% of σ_R for $^{20}Ne + ^{40}Ca$, instead of the 90% for $^{16}O + ^{40}Ca$.

The position and height of the s-wave interaction barrier and the nuclear potential at the barrier maximum deduced from the real optical potential are comparable with results from the other models as reported in Table II.

V. CONCLUSION

Cross sections for the complete fusion of ^{20}Ne with ^{40}Ca were measured by detecting the evaporation residues from the Zn compound nucleus decay with a gas-flow counter telescope. Discrepancies between the experimental angular distributions and the predictions from the simple evaporation model suggested large angular momentum effects. A more detailed study is desirable.

The fusion excitation curves could be reproduced by calculations using the proximity and the Siwek-Wilczynska-Wilczynski potentials, provided larger radii were used, namely, $C_i \approx 1.13 A^{1/3}$ fm. Such a variation of the radii does not contradict the physical content of the models. Indeed, Blocki *et al.*[7] have suggested that some variation of the proximity potential standard parameters, particularly the nuclear radii, may be necessary in order to take into account the individual nuclear properties of the colliding nuclei; this should also be true for the SWW potential. The results from the present work are in agreement with conclusions from a systematic analysis of the fusion data using the proximity potential.[21] Vaz and Alexander[21] have found that small changes in the parameters γ, b, and R are required to give reasonable fits to the experimental data; variations in γ or b have, however, much smaller effects than in R. The best fit increases ΔR plotted vs the charge product $Z_T Z_p$ scatter around an average curve having a broad maximum at about $Z_T Z_p = 200$, which is the value for the $^{20}Ne + ^{40}Ca$ system.

Although the ratio of the fusion to the total reaction cross section is noticeably lower for $^{20}Ne + ^{40}Ca$ than for $^{16}O + ^{40}Ca$, there is a consistency between their fusion data. Both data could be reproduced with nearly the same parameters within the framework of the proximity, the SWW, or the folding potential.

The elastic scattering data for $^{20}Ne + ^{40}Ca$ were analyzed in terms of the optical model using a four-parameter potential. When the strength of the potential real part was fixed to the value postulated in the SWW model, the interaction barrier characteristics deduced from the best-fit optical potential were comparable to that provided by the other models.

The authors wish to thank A. Maurice for dedicated technical assistance, and Dr. Y. Eyal for providing them with the EVA code.

[1] L. C. Vaz and J. M. Alexander, Phys. Rev. C 18, 833 (1978).
[2] J. R. Birkelund and J. R. Huizenga, Phys. Rev. C 17, 126 (1978).
[3] J. S. Blair, Phys. Rev. 108, 827 (1957).
[4] D. Glas and U. Mosel, Nucl. Phys. A237, 429 (1975).
[5] D. F. Geesaman, C. N. Davids, W. Henning, D. G. Kovar, K. E. Rehm, J. P. Schiffer, S. L. Tabor, and F. W. Prosser Jr., Phys. Rev. C 18, 284 (1978).
[6] Nguyen Van Sen, G. Ratel, R. Darves-Blanc, J. C. Gondrand, and F. Merchez, Phys. Rev. C 17, 639 (1978).
[7] J. Blocki, J. Randrup, W. J. Swiatecki, and C. F. Tsang, Ann. Phys. (N.Y.) 105, 427 (1977).
[8] K. Siwek-Wilczynska and J. Wilczynski, Phys. Lett. 74B, 313 (1978); 55B, 270 (1975).
[9] D. L. Hill and J. A. Wheeler, Phys. Rev. 89, 1102 (1953).

[10]D. M. Brink and N. Rowley, Nucl. Phys. A219, 79 (1974).
[11]Obtained from Union Carbide Corporation.
[12]A. J. Gorski and M. J. Fluss, Nucl. Instrum. Methods 115, 47 (1974).
[13]J. B. Moulton, J. E. Stephenson, R. P. Schmitt, and G. J. Wozniak, Nucl. Instrum. Methods 157, 325 (1978).
[14]L. C. Northcliffe and R. F. Schilling, Nucl. Data Tables A7, 233 (1970).
[15]Y. Eyal, M. Beckerman, R. Chechik, Z. Fraenkel, and H. Stocker, Phys. Rev. C 13, 1527 (1976).
[16]I. Dostrovsky, Z. Fraenkel, and G. Friedlander, Phys. Rev. 116, 683 (1959).
[17]C. Ngô, B. Tamain, M. Beiner, R. J. Lombard, D. Mas, and H. H. Deubler, Nucl. Phys. A252, 237, 1975.
[18]F. G. Perey, Phys. Rev. 131, 745 (1963), and private communication.
[19]Nguyen Van Sen, R. Darves-Blanc, F. Merchez, and J. C. Gondrand, Z. Phys. A276, 335 (1976).
[20]W. Scobel, A. Mignerey, M. Blann, and H. H. Gutbrod, Phys. Rev. C 11, 1701 (1975).
[21]L. C. Vaz and J. M. Alexander, Phys. Rev. C 18, 2152 (1978).
[22]See AIP document No. PAPS PRVCA 20-969-3 for 3 pages of tabulations of experimental data illustrated in Figs. 5 and 7. Order by PAPS number and journal reference from American Institute of Physics, Physics Auxiliary Publications Service, 335 East 45th Street, New York, New York 10017. The price is $1.50 for microfiche or $5 for photocopies. Airmail additional. Make checks payable to the American Institute of Physics. This material also appears in *Current Physics Microfilm*, the monthly microfilm edition of the complete set of journals published by AIP, on frames immediately following this journal article.